Contrast Enhancement of Dental Lesions by Light Source Optimisation

Joni Hyttinen[1 [0000−0003−1539−7445]], Pauli Fält[1 [0000−0003−4327−9104]], Laure Fauch[1 [0000−0002−3875−222X]], Anni Riepponen[2 [0000−0001−5254−4032]], Arja Kullaa[2 [0000−0001−8198−8185]], and Markku Hauta-Kasari[3 [0000−0002−5481−0004]]

[1] University of Eastern Finland, SIB Labs,
Yliopistokatu 2, P.O. Box 111, FI-80101 Joensuu, Finland
{joni.hyttinen,pauli.falt,laure.fauch}@uef.fi
[2] University of Eastern Finland, Institute of Dentistry,
Yliopistonranta 1 C, P.O. Box 1627, FI-70211 Kuopio, Finland
{anni.riepponen,arja.kullaa}@uef.fi
[3] University of Eastern Finland, School of Computing,
Yliopistokatu 2, P.O. Box 111, FI-80101 Joensuu, Finland
markku.hauta-kasari@uef.fi

Abstract. Dental lesions such as calculus and initial caries can be challenging to distinguish in RGB colour images due to a poor contrast. The visibility of dental lesions can be improved by using spectrally optimised light sources. In this paper, the optimal spectral shapes of illuminants for the visibility enhancement of various lesions are determined. These optimal spectral shapes are determined computationally by using spectral images captured from extracted human teeth, and numerical optimisation.

Keywords: Spectral imaging · Dentistry · Light sources · Optimisation · Visibility enhancement · Contrast

1 Introduction

Discerning some of the possible dental lesions from a healthy enamel can be challenging when inspecting intraoral RGB images of the teeth due to a low contrast between the lesion and tooth. This challenge has prompted several studies; however, they have concentrated on differences in the fluorescent properties of the teeth in comparison to plaque [1], caries [2], and calculus, both supragingival [3–6] and subgingival [7–9], and on optical coherence tomography (OCT) [10]. The OCT can be relatively expensive, its interferometric nature requires complicated optical set-up, and can image only a small area at a time. On the other hand, full-spectral range fluorescence imaging requires not only exposure to UV-light, but also multiple measurements: for each excitation wavelength, an emission spectrum must be measured. If the fluorescence is ignored, however, a single measurement can produce a spectral image with no need for UV-exposure.

The final authenticated version is available online at https://doi.org/10.1007/978-3-319-94211-7_54

Our long-term aim is to build cost-effective and user-friendly imaging systems for use in dental clinics. We intend to achieve this by using spectral image data to design spectrally optimal light sources for imaging systems. A spectral reflectance image may contain hundreds of intensity channels over a desired wavelength range, while an RGB colour image contains three intensity channels for red, green, and blue colours. These spectral images are also called data cubes due to the extensive amount of intensity information stored in them, while the process of acquiring these has been named spectral imaging. This intensity information can be used for contrast optimisation.

In this study, spectral images of extracted human teeth were used to determine the spectral shapes of such light sources which maximise the contrast between a lesion and an intact tooth area. The contrast optimisation was performed by the particle swarm optimisation method (PSO), which has been earlier applied to a similar problem regarding diabetic retinopathy lesions [11, 12]. To authors' best knowledge, this approach has no earlier application in dentistry.

2 Methods

The spectral images of extracted human teeth had been captured in the wavelength range 390–1000 nm with an average step size of 2.55 nm (240 channels in total), which was chosen as the allowed optimisation range. These images were captured using a Specim VNIR imaging spectrograph (Specim, Spectral Imaging Ltd., Finland). The teeth had been extracted at, and donated to the Dental School Clinic of the University of Eastern Finland (Kuopio, Finland) for educational and research purposes. Dental experts hand-marked the ground truth data on photographs of the sample teeth. On the photographs of the occlusal surfaces, markings were available and used for initial and dentine caries, calculus, erosion and attrition, and stains. The views from the sides of the teeth had separate markings for two types of calculus: white and dark calculus.

Spectral images' spatial resolution varied as the samples had been imaged in groups and thus the individual images had been cropped from larger images. These data cubes were the samples' spectral reflectance images $R_{\text{sample}}(x, y, \lambda)$ that have been calculated as visualised on the upper half of Fig. 1. These images were then used to calculate the reference images $I_{\text{ref}}(x, y)$ and the contrast optimised images $I_{\text{opt}}(x, y)$ as if they were illuminated by the reference and optimal illuminants. The CIE D65 daylight illuminant was chosen as the reference illuminant. This process is visualised on the left side of Fig. 1.

The spectral distribution $s_{\text{opt}}(\lambda)$ of an optimal illuminant was assumed to be a convex combination of N separate α_i-weighted narrow ($\sigma = 75$) Gaussian signals $s_i(\lambda)$. The number of signals N was chosen to match the number of channels ($N = 240$). The weights α_i, on the other hand, were required to be positive or zero valued, so that their sum equalled one. These values were determined by the PSO process explained below.

In addition to a spectral reflectance image and an illuminant, the reconstruction of an image required an observer. The observer chosen for the reference im-

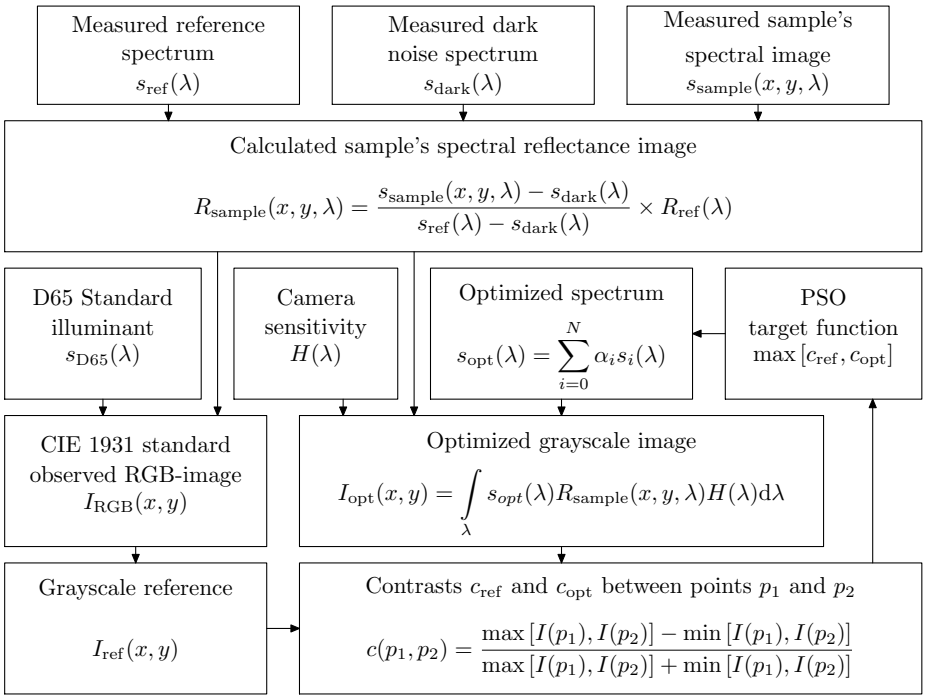

Fig. 1. The process for obtaining a spectral reflectance image $R_{\mathrm{sample}}(x, y, \lambda)$, a base reference $I_{\mathrm{ref}}(x, y)$, and an optimised image $I_{\mathrm{opt}}(x, y)$. $R_{\mathrm{ref}}(\lambda)$ refers to the reference sample's spectral reflectance. The p_1 and p_2, $p_n = (x_n, y_n)$, denote the contrast comparison points within the same image, while x and y are pixel coordinates.

age was the CIE 1931 standard observer, and for the optimal image, a quantum efficiency $H(\lambda)$ imitating a monochrome camera. The function was selected to be a Gaussian distribution centred at 550 nm with wide variance ($\sigma = 25000$) as presented in Fig. 2a. This distribution approximated the shape of the quantum efficiency of several commercial monochrome cameras.

The visibility of lesions on the surface of a tooth is determined by the ratio of the average reflected intensity of a region p_1 within a lesion, and the average reflected intensity of a nearby non-lesion area, p_2, as the Michelson contrast [13] $c(p_1, p_2)$ presented in Fig. 1. The intensities of selected pixel coordinates p_n were determined as the average of the intensities in a 7×7 rectangle centred on the coordinates.

The light source optimisation was performed by the particle swarm optimisation (PSO) [11]. It employs a "swarm" of particles travelling in the solution space looking for the optimal value of a cost function. Each particle i has a position $\boldsymbol{x}_i$, a velocity $\boldsymbol{v}_i$, and a local best position $\boldsymbol{x}_l$ denoting the optimal value the particular particle has found. Additionally, the swarm maintains a global best position $\boldsymbol{x}_g$ denoting the optimal value the swarm as a whole has found. All of

these variables are updated on each iteration step t. The position and velocity are updated as per equations

$$\boldsymbol{v}_i(t+1) = C_0\boldsymbol{v}_i(t) + C_1\boldsymbol{r}_1(t)\left[\boldsymbol{x}_l(t) - \boldsymbol{x}_i(t)\right] + C_2\boldsymbol{r}_2(t)\left[\boldsymbol{x}_g - \boldsymbol{x}_i(t)\right] \quad , \tag{1a}$$

$$\boldsymbol{x}_i(t+1) = \boldsymbol{x}_i(t) + \boldsymbol{v}_i(t+1) \quad , \tag{1b}$$

where C_0 is an inertia term, C_1 and C_2 determine the weights of the local and global bests, and $\boldsymbol{r}_1(t)$ and $\boldsymbol{r}_2(t)$ contain new uniformly distributed random numbers in the range $[0, 1]$ for each iteration step t [11, 12].

The values $C_0 = 0.95$, $C_1 = 2.0$, and $C_2 = 2.0$ were deemed suitable for the optimisation process which was run for 200 iterations, although in most cases it converged into an optimal solution in half of that. The process employed 5000 particles for each comparison point-pair (p_1, p_2).

Once the optimal illuminant spectra $s_{\mathrm{opt}}(\lambda)$ for all comparison pairs of a lesion type had been found, normalised cumulative spectra $s_{\mathrm{cum}}(\lambda)$ were computed for all lesion types. These cumulative spectra were then used to compute cumulative contributions of each wavelength channel, and the final, outlier-free spectra $s_{\mathrm{con}}(\lambda)$ were generated by constricting the number of channels to only those contributing the first 50% of all contributions.

3 Results and Discussion

The optimisation process favoured light sources which consisted of a single Gaussian, to the point that every chosen point-pair for contrast optimisation converged to a one. A cumulated spectrum was calculated for each of these point-pairs. Some of the spectra, as indicated by the graphs in Fig. 2, exhibit significant dispersion as the comparison pairs found multiple optimal solutions. For example, white calculus spectra (in Fig. 2f) shows several significant peaks.

The crown enamel and root dentine comparison provided divisive results as the optimal contrast can be found peaking approximately at 400 nm, 500 nm, and 600 nm depending on sample, as can be seen in Fig. 2b. The contrast at 400 nm peak illumination caused the root to show as the darker part while the crown was the brighter one. This arrangement is reversed, however, at the two other peaks. Despite of that, the cumulative spectrum of Fig. 2b can still produce noticeable contrast as evidenced on Fig. 4c. This illuminant enhances contrast from $3 \pm 3\%$ to $11 \pm 8\%$ on average over all test points. The contributor-corrected illuminant was constructed from 16 most significant channels, and is presented in Fig. 2c. This illuminant enhances contrast to $18 \pm 13\%$, but no improvement is noticeable in Fig. 4d.

Two teeth had stains on their occlusal surface with an initial contrast of $6 \pm 2\%$ against crown. After optimisation, the cumulative illuminant peaking at 406 nm, Fig. 2g, provided an increase to $43 \pm 15\%$ as presented in Fig. 4k. The contributor-constricted illuminant constructed from five channels and presented in Fig. 2l did not have any practical effect providing a contrast value $44 \pm 15\%$ as evidenced in Fig. 4l. These same two teeth were also affected by erosion or

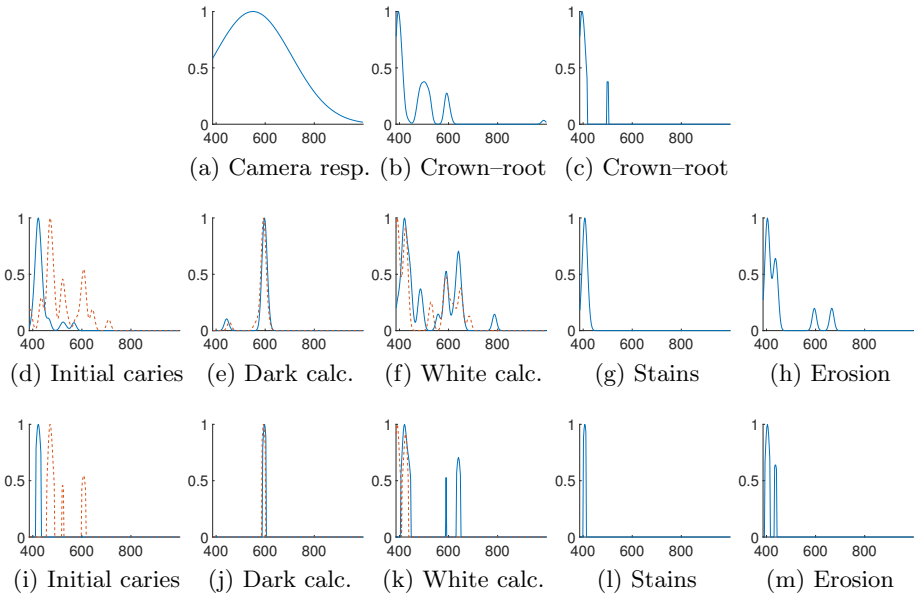

(a) Camera resp. (b) Crown–root (c) Crown–root

(d) Initial caries (e) Dark calc. (f) White calc. (g) Stains (h) Erosion

(i) Initial caries (j) Dark calc. (k) White calc. (l) Stains (m) Erosion

Fig. 2. (a) The assumed Gaussian sensitivity curve for a monochrome camera. (b), (d)–(h) Optimal illuminant spectra as the normalised sums of all individual optimally weighted Gaussian distributions. (c), (i)–(m) Optimal illuminants constructed from channels contributing the first 50% of all contributions. The solid line refers to lesion–enamel comparison and dashed line to lesion–dentine comparison where applicable. All graphs present normalized intensities as a function of wavelength.

attrition. The starting contrast value was $3 \pm 2\%$, while the cumulative spectrum as per Fig. 2h improved it to $13 \pm 12\%$ in Fig. 4g. Finally, the contribution-constricted illuminant produced $19 \pm 16\%$ contrast in Fig. 4h. Surprisingly, the erosion is more visible on the stained tooth image in Fig. 4l.

In the ground truth data, initial caries was marked on 21 teeth; 14 of which had it on occlusal surfaces and seven on a side surface. For this lesion type, the cumulative light source in Fig. 2d had a centre peak at 423 nm giving the contrast maximum of $50 \pm 20\%$ when the lesion is compared against the crown enamel. The original contrast was only $20 \pm 10\%$ meaning a $330 \pm 190\%$ increase as evidenced in Fig. 3c. The contributor-constricted illuminant in Fig. 2i required only nine channels. As could be expected, the cumulative and constricted illuminants are sufficiently similar that the images illuminated by the latter in Figs. 3d and 3h has no noticeable difference to the one illuminated by the former in Figs. 3c and 3g.

When compared to the root dentine, the cumulative spectrum on Fig. 2i had several peaks and maxima spread from 400 nm up to 700 nm range, which could indicate that the comparison point-pairs chosen for optimisation may have been comparing the caries points to other kinds of lesions instead of intact dentine. It

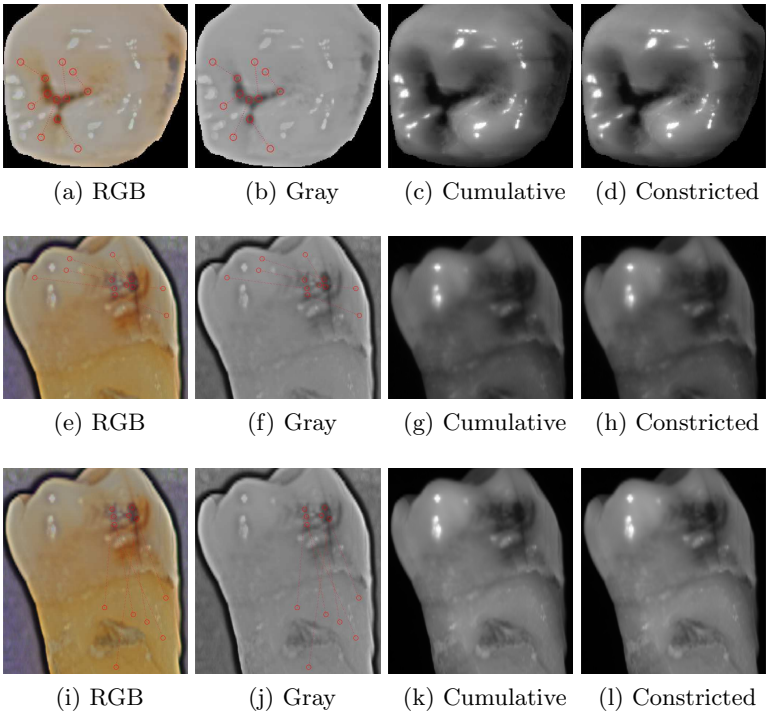

(a) RGB (b) Gray (c) Cumulative (d) Constricted

(e) RGB (f) Gray (g) Cumulative (h) Constricted

(i) RGB (j) Gray (k) Cumulative (l) Constricted

Fig. 3. Contrast enhancement of initial caries on (a)–(d) occlusal surface, on (e)–(h) side against enamel, and on (i)–(l) side against root on the same tooth. The connected red circles denote the comparison point-pairs.

is also worth noting that the enamel comparison included 21 teeth, the dentine comparison only seven. The original contrast for root dentine comparison was $18\pm14\%$, while the cumulative illuminant enhanced it to $36\pm21\%$ in Figs. 3j and 3k. The contributor-constricted illuminant of Fig. 2d was constructed from 23 channels generating peaks at 470, 522, and 607 nm; it provides no improvement, however. While the differences between the cumulative and constricted illuminants have no significant difference, when comparing them to enamel versions in Figs. 3g and 3h, observable differences emerge. Namely, the enamel becomes lighter, and a dark oval mark on the crown becomes more notable in Fig. 3l.

Dark calculus had a clear peak at 598 nm and 593 nm for enamel and dentine comparisons, respectively, in Figs. 2e. These nearly inseparable peaks contribute the most with only six wavelength channels centred on the peak, which is why the outlier-free version discards the local maximum at 443 nm and narrows the peak on Fig. 2j. The effect of the cumulative illuminant is presented in Fig. 5c and of the contribution-constricted illuminant in Fig. 5d. These images not only show dark calculus as the dark area on the root, but also some white calculus with slightly increased contrast mostly on account of darker dark calculus.

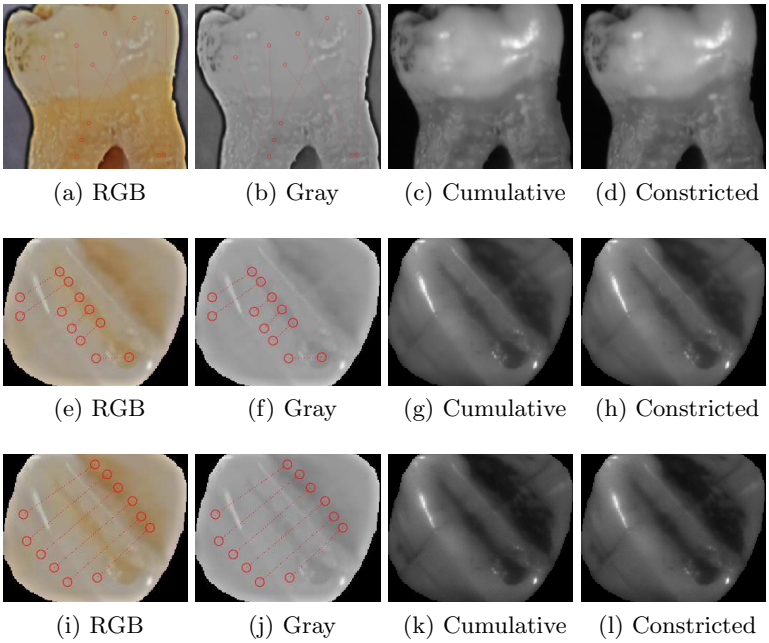

(a) RGB (b) Gray (c) Cumulative (d) Constricted

(e) RGB (f) Gray (g) Cumulative (h) Constricted

(i) RGB (j) Gray (k) Cumulative (l) Constricted

Fig. 4. Contrast enhancement between crown enamel and (a)-(d) root dentine, (e)-(h) erosion or attrition, (i)-(l) stain. The connected red circles denote the comparison point-pairs.

White calculus had several cases where the optimal contrast of a pair-point was approximately located in the vicinity of 400, 500, or 600 nm wavelengths, leading to a dispersed cumulative spectrum in Fig. 2f for crown enamel and to a lesser extent for root dentine comparisons. The cumulative illuminant, Fig. 2f, increased the contrast from $4 \pm 3\%$ to $10 \pm 6\%$ with enamel and to $12 \pm 6\%$ with dentine comparison. The constricted illuminant, Fig. 2k, occupied 25 most significant channels for crown, and 20 channels for root comparison, and improves the contrast to $12 \pm 8\%$ with enamel and to $21 \pm 14\%$ with dentine.

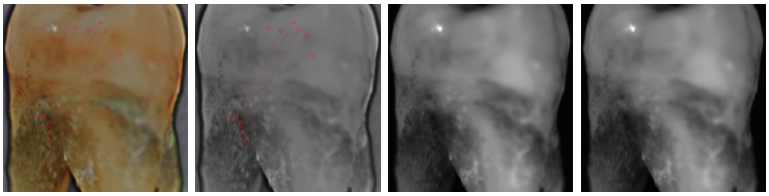

(a) RGB (b) Gray (c) Cumulative (d) Constricted

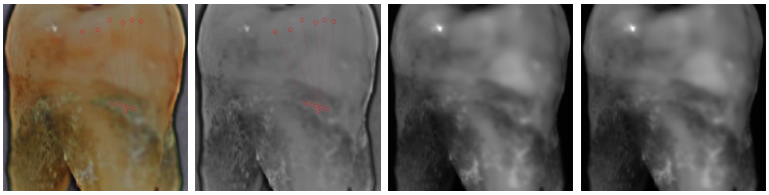

(e) RGB (f) Gray (g) Cumulative (h) Constricted

Fig. 5. Contrast enhancement between crown enamel and (a)-(d) dark calculus, (e)-(h) white calculus. The connected red circles denote the comparison point-pairs.

4 Conclusions

Optimal illuminants for contrast enhancement of initial caries, dark and white calculus, erosion and staining on extracted human teeth were determined utilising crown enamel or root dentine as comparison. Notably, most of the illuminants had their most significant peak near 400 nm, with the exception of dark calculus at 600 nm. While these illuminants increased contrast, their error margins were rather wide over the sample points expanding the cumulative spectrum, and so producing multiple peaks for the contribution-constricted version. The presented spectra could be implemented as contrast-optimising light sources or optical filters for each lesion type.

Acknowledgements This study was funded by Business Finland and the European Regional Development Fund (ERDF) (funding decision 4465/31/2017).

References

1. Joseph, B., Prasanth, C.S., Jayanthi, J.L., Presanthila, J. and Subhash, N.: Detection and quantification of dental plaque based on laser-induced autofluorescence intensity ratio values. J. Biomed. Opt. **20**(4) 048001-1–048001-10 (2015). doi: https://doi.org/10.1117/1.JBO.20.4.048001
2. Son, S.-A., Jung, K.-H., Ko, C.-C. and Kwon, Y.H.: Spectral characteristics of caries-related auto-fluorescence spectra and their use for diagnosis of caries stage. J. Biomed. Opt. **21**(1) 015001-1–015001-8 (2016). doi: https://doi.org/10.1117/1.JBO.21.1.015001

3. Buchalla, W., Lennon, A.M. and Attin, T.: Fluorescence spectroscopy of dental calculus. J. Periodont. Res. **39** 327–332 (2004). doi: https://doi.org/10.1111/j.1600-0765.2004.00747.x
4. Qin, Y.L., Luan, X.L., Bi, L.J., Lü, Z., Sheng, Y.Q., Somesfalean, G., Zhou, C.N. and Zhang, Z.G.: Real-time detection of dental calculus by blue-LED-induced fluorescence spectroscopy. J. Photochem. Photobiol. B-Biol. **87** 88–94 (2007). doi: https://doi.org/10.1016/j.jphotobiol.2007.03.002
5. Gonchukov, S., Biryukova, T., Sukhinina, A. and Vdovin, Y.: Fluorescence detection of dental calculus. Laser Phys. Lett. **7**(11) 812–816 (2010). doi: https://doi.org/10.1002/lapl.201010065
6. Lee, Y.-K.: Fluorescence properties of human teeth and dental calculus for clinical applications. J. Biomed. Opt. **20**(4) 040901-1–040901-8 (2015). doi: https://doi.org/10.1117/1.JBO.20.4.040901
7. Kurihara, E., Koseki, T., Gohara, K., Nishihara, T., Ansai, T. and Takehara, T.: Detection of subgingival calculus and dentine caries by laser fluorescence. J. Periodont. Res. **39** 59–65 (2004). doi: https://doi.org/10.1111/j.1600-0765.2004.00712.x
8. Badran, Z., Demoersman, J., Struillou, X., Boutigny, H., Weiss, P. and Soueidan, A.: Laser-Induced Fluorescence for Subgingival Calculus Detection: Scientific Rational and Clinical Application in Periodontology. Photomed. Laser Surg. **29**(9) 593–596 (2011). doi: https://doi.org/10.1089/pho.2010.2951
9. Shakibaie, F. and Walsh, L.J.: Surface area and volume determination of subgingival calculus using laser fluorescence. Lasers Med. Sci. **29** 519–524 (2014). doi: https://doi.org/10.1007/s10103-012-1242-9
10. Hsiesh, Y.-S., Ho, Y.-C., Lee, S.-Y., Chuang, C.-C., Tsai, J., Lin, K.-F. and Sun, C.-W.: Dental Optical Coherence Tomography. Sensors **13** 8928–8949 (2013). doi: https://doi.org/10.3390/s130708928
11. Bratton, D., Kennedy, J.: Defining a standard for particle swarm optimization. 2007 IEEE Swarm Intelligence Symposium 120–127 (2007). doi: https://doi.org/10.1109/SIS.2007.368035
12. Fält, P., Hauta-Kasari, M., Sorri, I., Kalesnykiene, V., Pietilä, J. and Uusitalo, H.: Spectral Imaging of the Human Retina and Computationally Determined Optimal Illuminants for Diabetic Retinopathy Lesion Detection. J. Imaging Sci. Technol. **55**(3) 030509-1–030509-10 (2011). doi: https://doi.org/10.2352/J.ImagingSci.Technol.2011.55.3.030509
13. Michelson, A.A.: Studies in Optics. The University of Chicago Press (1927)